

---

# CROSS-DOMAIN LONG-TERM FORECASTING: RADIATION DOSE FROM SPARSE NEUTRON SENSOR VIA SPATIO-TEMPORAL OPERATOR NETWORK

---

PREPRINT

**Jay Phil Yoo**

Nuclear, Plasma & Radiological Engineering  
 University of Illinois at Urbana-Champaign  
 Urbana, IL 61801, USA  
 roysam@illinois.edu

**Kazuma Kobayashi**

Nuclear, Plasma & Radiological Engineering  
 National Center for Supercomputing Applications  
 University of Illinois at Urbana-Champaign  
 Urbana, IL 61801, USA  
 kazumak2@illinois.edu

**Souvik Chakraborty**

Department of Applied Mechanics  
 Yardi School of Artificial Intelligence  
 Indian Institute of Technology Delhi  
 New Delhi, India  
 souvik@am.iitd.ac.in

**Syed Bahauddin Alam**

Nuclear, Plasma & Radiological Engineering  
 National Center for Supercomputing Applications  
 University of Illinois at Urbana-Champaign  
 Urbana, IL 61801, USA  
 alams@illinois.edu

October 22, 2025

**ABSTRACT**

Forecasting unobservable physical quantities from sparse, cross-domain sensor data is a central unsolved problem in scientific machine learning. Existing neural operators and large-scale forecasters rely on dense, co-located input–output fields and short temporal contexts, assumptions that fail in real-world systems where sensing and prediction occur on distinct physical manifolds and over long timescales. We introduce the **Spatio-Temporal Operator Network (STONe)**, a non-autoregressive neural operator that learns a stable functional mapping between heterogeneous domains. By directly inferring high-altitude radiation dose fields from sparse ground-based neutron measurements, STONe demonstrates that operator learning can generalize beyond shared-domain settings. It defines a nonlinear operator between sensor and target manifolds that remains stable over long forecasting horizons without iterative recurrence. This challenges the conventional view that operator learning requires domain alignment or autoregressive propagation. Trained on 23 years of global neutron data, STONe achieves accurate 180-day forecasts with millisecond inference latency. The framework establishes a general principle for cross-domain operator inference, enabling real-time prediction of complex spatiotemporal fields in physics, climate, and energy systems.

## 1 Introduction

Galactic Cosmic Radiation (GCR) presents underappreciated risks at Earth’s surface and particularly at aviation altitudes. While Earth’s atmosphere and magnetic field provide substantial protection, cosmic radiation exposure increases dramatically with altitude, creating substantial occupational health concerns for aircrew and frequent flyers. At typical commercial aviation altitudes (10–12 km), radiation dose rates can be 50–100 times higher than at sea level, with aircrew receiving annual doses comparable to or exceeding those of nuclear industry workers [1, 2]. The International Commission on Radiological Protection has classified aircrew as radiation workers since 1990, recognizing the significant occupational exposure risks. The health implications extend beyond occupational concerns to affect millions of air travelers annually. Pregnant women face particular risks, as fetal tissue is highly radiosensitive, with

potential for developmental abnormalities and increased cancer risk [3]. For frequent business travelers and aircrew, cumulative exposures over career spans can approach or exceed recommended annual limits for radiation workers. Yet, despite decades of progress in cosmic ray transport modeling, we still lack the ability to forecast high-altitude radiation fields in real time: a failure rooted not in physics, but in the limitations of our current predictive paradigms.

Weather forecasting has traditionally been dominated by Numerical Weather Prediction (NWP) methods, which often employ Monte Carlo sampling to generate an ensemble of trajectories for their predictions. While this method provides accurate and reliable forecasts with some notion of uncertainty quantification, it suffers from immense computational resource requirements when scaled, and it requires large amounts of data to ensure accuracy. Over the past few years, machine learning-based forecasters have begun to challenge this paradigm, demonstrating that data-driven representations of atmospheric dynamics can match or even exceed the skill of traditional NWP models at a fraction of the computational cost [4, 5, 6, 7, 8]. Models such as FourCastNet and GraphCast capture global-scale weather evolution through learned operators rather than numerical integration, signaling a fundamental transition from equation-driven to data-driven forecasting. NeuralGCM provides a hybrid method of NWP and machine learning-based weather prediction (MLWP), at the cost of forecasting resolution [7]. Gencast [8], the first MLWP to surpass the NWP model ENS, employs a weak second-order Markov assumption to generate a probabilistic approach using a diffusion model. Yet, despite these advances, all current architectures share a common structural assumption: the input and output fields must exist on the same spatial grid and within the same physical domain. This constraint fundamentally limits their applicability to problems where sensing and prediction occur in different regimes, a gap that becomes particularly critical for radiation dose forecasting.

Radiation dose forecasting presents a unique challenge. Unlike weather forecasting, the input data and target data lie in different physical domains due to the cascading nature of GCR. This domain mismatch means we can't directly measure the property of interest, the radiation dose, in the same way we can measure wind speed or temperature. Moreover, a limited number of ground-based neutron sensors provide sparse spatial coverage. Meanwhile, physics-based atmospheric cascade models require hours to days for accurate forecasting, which is far too slow for flight planning and real-time route optimization. This gap leaves airlines, pilots, and passengers vulnerable to unnecessary radiation exposure that could be mitigated through informed decision-making based on accurate, real-time radiation forecasts [9]. Unlike conventional atmospheric variables, radiation dose cannot be expressed as a direct observable; it must be inferred through a cascade process that couples primary cosmic ray spectra, geomagnetic modulation, and atmospheric transport. Ground neutron measurements are therefore proxies, not measurements of the field itself. This creates a fundamental epistemic divide between what can be sensed and what must be predicted.

The challenge is compounded by the complex, multi-scale nature of cosmic radiation transport through Earth's atmosphere. Primary cosmic rays interact with atmospheric nuclei to produce extensive air showers of secondary particles, creating radiation fields that vary significantly with altitude, latitude, solar activity, and atmospheric conditions [10]. Geomagnetic field variations, solar modulation, and atmospheric density changes introduce temporal variability that spans timescales from minutes (during geomagnetic storms) to years (solar cycle variations). Accurate forecasting requires integrating these diverse physical processes in real-time: a computational challenge that has historically limited operational radiation forecasting capabilities.

Traditional approaches to this challenge fall into two primary paradigms: first-principles modeling and data-driven discovery. Physics-based models rely on Monte Carlo simulations of particle cascades through detailed atmospheric models, offering high-fidelity predictions at a prohibitive computational cost that precludes real-time operation. In contrast, the expansion of global radiation monitoring networks has enabled the development of data-driven approaches that learn system dynamics directly from observational data. Early efforts focused on statistical correlations and empirical models, such as the Proper Orthogonal Decomposition (POD) and the Dynamic Mode Decomposition (DMD) [11, 12, 13], but these approaches struggle with the nonlinear, multi-scale dynamics of atmospheric radiation transport. More recent equation discovery methods, including Sparse Identification of Nonlinear Dynamics (SINDy) [14] and its extension to PDEs (PDE-FIND) [15], leverage sparse regression to identify the few critical terms in a library of candidate functions that describe the system's dynamics. These equation discovery methods produce parsimonious, interpretable models that can generalize beyond the training data. However, they rely on the existence of an explicit governing equation in a known coordinate frame, an assumption that collapses for systems like GCR cascades, where the mapping between observables and latent variables is both nonlinear and non-local. In such settings, the "operator" cannot be expressed in closed form, and it must be learned as a functional mapping between domains.

Neural operator frameworks represent a paradigm shift, learning solution operators that map input functions (e.g., initial conditions, boundary conditions, or forcing terms) to output functions (the system's state at a later time) rather than discovering the explicit differential operator (i.e., the equation). Neural operator frameworks enable surrogate models that outperform conventional finite-volume and finite-element methods in terms of speed and generalization. Recent advances, including Deep Operator Networks (DeepONet) [16] and the Fourier Neural Operator (FNO) [17],

have shown strong potential for real-time full-field predictions in nuclear and radiation systems [18, 19, 20]. Yet, their foundational design still presumes shared-domain mappings; they remain intra-domain surrogates, not cross-domain inferences.

For time-dependent systems, several neural operator forecasting paradigms exist. Autoregressive models, which propagate solutions step-by-step by recursively feeding predicted states as inputs for subsequent predictions [16, 17], offer flexibility in handling variable time horizons and can leverage the Markovian property of dynamical systems. The autoregressive approach's primary strength lies in computational efficiency during training, as it focuses on short-term mappings, and it naturally aligns with the causal evolution of PDEs. However, they are highly susceptible to error accumulation over long horizons, where small approximation errors compound, leading to instability and divergence from ground truth, particularly in chaotic or stiff systems [21, 22]. This limitation renders them unreliable for extended forecasting without the use of additional stabilization techniques. More critically, all autoregressive frameworks implicitly assume that the system's future state can be expressed within the same coordinate basis as its input: a hidden but restrictive assumption that prevents learning across distinct sensing and prediction domains.

An alternative is the sequence-to-sequence model, which predicts entire trajectories in a single pass, mapping initial conditions directly to spatiotemporal solutions over fixed horizons [23, 24, 25]. This approach reduces inference-time latency for predictions and has the ability to capture global patterns without iterative feedback loops. Nevertheless, training such models demands substantial computational resources due to the high-dimensional output space, and they lack inherent mechanisms to enforce physical constraints. More recently, temporal physics-integrated models, such as TI(L)-DeepONet [22], address these gaps by embedding numerical integrators (e.g., Runge-Kutta schemes) into the operator learning process to approximate time derivatives rather than states directly. **None address the deeper issue: the need to learn stable forecasting operators across physically disjoint manifolds.**

The limitations in existing data-driven paradigms prevent state-of-the-art models with proven success in weather forecasting from being directly applied to the radiation dose problem. For instance, FourCastNet [5] leverages FNO for rapid, high-resolution weather prediction, while GraphCast uses a Graph Neural Network (GNN) [26, 6] to achieve high accuracy in medium-range forecasting. However, both architectures are fundamentally intra-domain: they rely on autoregressive, field-to-field propagation within a structured grid, making them incompatible with sparse, cross-domain data. This incompatibility is not a technical obstacle but a theoretical one: the absence of a framework that can stably connect non-coincident sensor and prediction spaces over extended horizons.

Motivated by **this gap**, we propose a non-autoregressive neural operator framework designed specifically for **forecasting in sparse, cross-domain settings**. Our approach bypasses the architectural constraints of existing models by learning a direct sequence-to-sequence operator. This operator explicitly maps a time series of sparse, irregularly distributed sensor measurements to the entire future spatiotemporal evolution of the dense output field in a single forward pass.

The proposed **Spatio-Temporal Operator Network (STONe)** framework extends the Sequential Deep Operator Network (S-DeepONet) [27] into a new regime of **cross-domain operator learning**. STONe integrates recurrent and attention-based temporal encoders with a coordinate-conditioned trunk network to forecast entire spatiotemporal field trajectories directly from sparse and heterogeneous sensor measurements. Its **non-autoregressive architecture** enables long-horizon stability by eliminating iterative feedback, while its **operator decomposition**, consisting of a branch for sensor-sequence encoding and a trunk for field reconstruction, **resolves domain mismatch natively** without intermediate data-mapping steps. **STONe establishes a stable cross-domain functional mapping over extended forecasting windows, directly challenging the long-standing assumption that operator learning must rely on shared domains or autoregressive recurrence.** This formulation positions STONe as a general operator framework for scientific forecasting across physically disjoint manifolds.

More broadly, the adoption of operator-learning frameworks for scientific modeling paves the way for transformative applications in various sectors [28, 29, 30, 31, 32]. **This work departs fundamentally from conventional operator paradigms by introducing a non-autoregressive, cross-domain operator formulation that learns a direct functional mapping between distinct physical manifolds.** Unlike incremental advances that focus on accuracy or architectural depth, this paradigm redefines what an operator represents in scientific forecasting: **not a propagator constrained by geometry, but a universal map that connects sparse, indirect observations to unobservable physical fields.** In this sense, STONe extends the theoretical scope of operator learning from approximating PDE solutions to reconstructing latent dynamical systems that were previously inaccessible to direct measurement.

The timeliness of this paradigm arises from three converging developments that make cross-domain operator learning feasible for the first time. First, the global availability of multi-decadal neutron monitor data provides a uniquely rich, continuous dataset for learning the statistical and physical coupling between ground and atmospheric radiation

domains. Second, the maturation of sequence-modeling architectures such as GRUs, LSTMs, and Transformers enables the capture of long-range temporal dependencies from sparse sensor histories, a capability essential for stable operator learning across timescales. Third, advances in high-performance and energy-efficient AI hardware now permit sub-millisecond inference latency, allowing real-time deployment of operator models in operational environments such as flight planning and radiation monitoring. Together, these developments create the precise technological and data landscape in which cross-domain operator learning can be realized at scale, marking a decisive turning point for scientific forecasting.

**Key contributions include:**

- **From Domain-Matched to Cross-Domain Operator Learning:** Existing neural operator forecasting frameworks assume that input and output functions are defined on the same spatial or temporal grid, which fails in real-world systems where sensing and prediction occur on distinct manifolds. The proposed **Spatio-Temporal Operator Network (STONE)** defines a stable nonlinear operator  $\mathcal{G} : \mathcal{H}_s \rightarrow \mathcal{H}_t$  that learns mappings between physically distinct manifolds, enabling cross-domain operator learning directly from sparse, misaligned sensor data.
- **From Forward Simulation to Inverse Operator Inference:** Traditional PDE-based solvers and learned operators are restricted to forward physics simulations that remain computationally prohibitive for real-time inference. STONE reframes forecasting as an **inverse operator problem**, learning mappings from observable proxies to latent fields without explicitly resolving governing equations, while achieving real-time feasibility.
- **From Iterative Autoregression to Non-Autoregressive Stability:** Sequence-based architectures such as LSTMs and Transformers often accumulate prediction errors over long temporal horizons. STONE introduces a **non-autoregressive operator formulation** that predicts the full spatiotemporal trajectory in a single pass, eliminating recursive feedback and achieving stable 180-day forecasting with no compounding error.
- **From High-Fidelity Simulation to Real-Time Inference:** Physics-based atmospheric cascade simulations require hours to days for full radiation transport propagation, preventing operational use. STONE learns a direct functional mapping from sparse proxies to global fields, achieving **millisecond-scale inference latency** with high spatial fidelity, providing an operationally viable surrogate for radiation dose forecasting.
- **From Domain-Specific Models to a Universal Operator Paradigm:** Existing operator-learning architectures are often tailored to specific physical systems or data modalities. STONE establishes a **universal cross-domain operator framework** that generalizes across scientific domains such as climate modeling, geophysical inversion, representing a foundational step toward general-purpose operator models for data-sparse systems.

## 2 Methodology

### 2.1 Data Preparation and Preprocessing

Accurately estimating cosmic radiation dose is critical for aviation safety and space weather monitoring, but traditional physics-based simulations introduce latency for real-time applications. To address this, we reframe the task as a data-driven inverse problem [33]. Instead of simulating the complex chain of events from primary cosmic rays to radiation dose, our model learns a direct mapping from sparse, ground-based neutron sensor measurements to high-resolution global dose fields (Figure 1) solving the inverse problem.

The forward modeling approach simulates the causal chain from primary cosmic ray fluxes ( $\Phi$ ) to downstream effects like ground-level neutron counts and dose rates. For a given sensor  $n$ , the neutron count  $Y_n$  is a function of the primary flux, atmospheric conditions ( $A$ ), the geomagnetic field ( $G$ ), and altitude ( $h$ ):

$$Y_n = f_n(\Phi, A, G, h) \in \mathbb{R}^T \quad (1)$$

where  $f_n$  represents the complex particle transport physics and  $T$  is the number of time steps. For a network of  $S$  sensors, the combined data form a matrix  $\mathbf{Y} = \{Y_1, \dots, Y_N\} \in \mathbb{R}^{T \times N}$ .

Similarly, the effective dose rate  $X_j$  at a specific location  $j$  is determined by the same physical drivers, modeled by a function  $g_j$ :

$$X_j = g_j(\Phi, A, G, h) \quad (2)$$

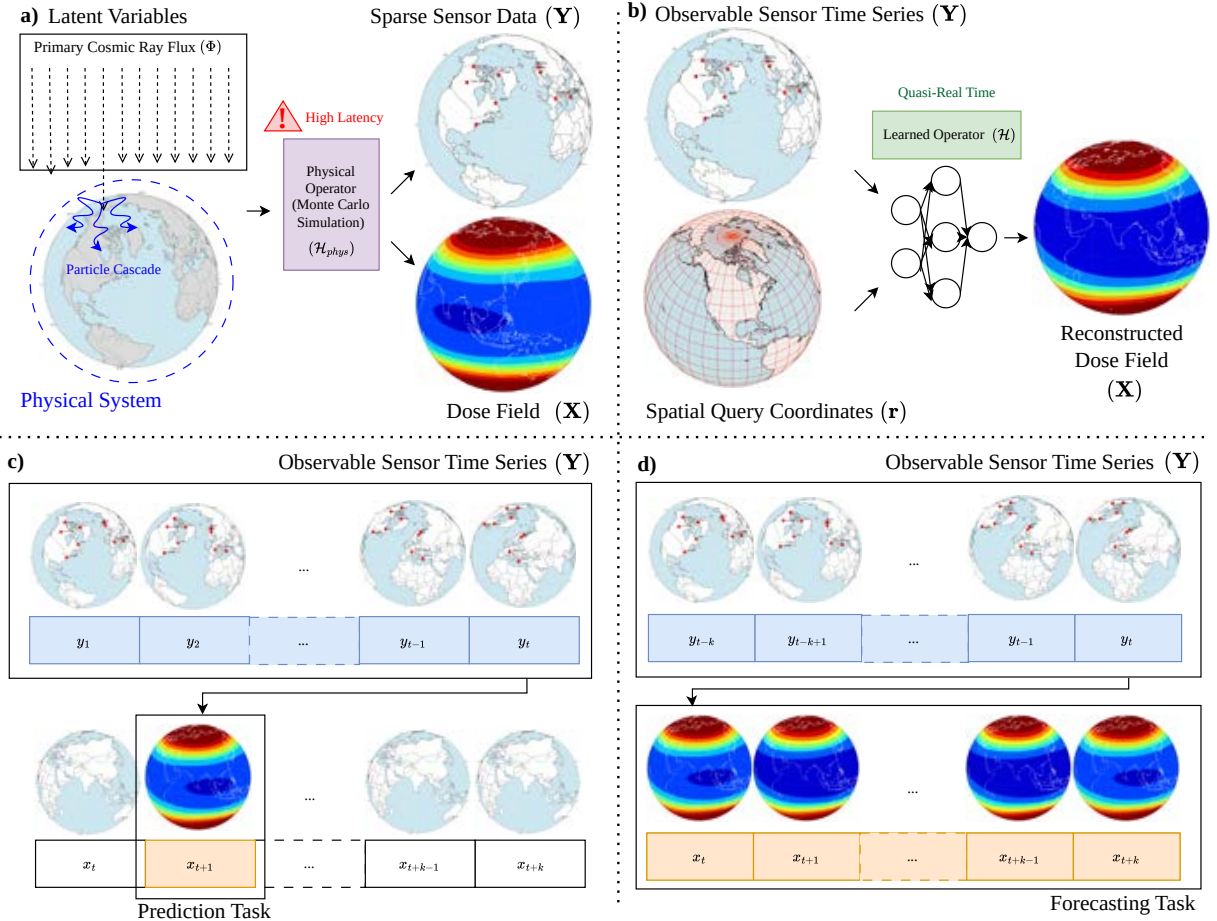


**Figure 1: Conceptual framework and STONe forecasting approach for data-driven radiation dose reconstruction.** The figure illustrates the transition from a traditional physics-based forward model to a learned inverse operator enabling real-time global dose forecast. **a)** Forward problem (physics-based simulation): Unobservable latent drivers, primarily the primary cosmic-ray flux ( $\Phi$ ), interact with Earth's atmosphere and geomagnetic field. High-fidelity Monte Carlo transport is necessary to model the ensuing particle cascades, resulting in sparse ground-based neutron monitor time series ( $\mathbf{Y}$ ) and high-altitude radiation dose fields ( $\mathbf{X}$ ). Evaluating the latent physical operator  $\mathcal{H}_{phys}$  incurs substantial computational latency. **b)** Inverse problem (learned spatiotemporal operator): A neural operator  $\mathcal{H}$  maps observable sensor time series ( $\mathbf{Y}$ ) and spatial query coordinates ( $\mathbf{r}$ ) directly to reconstructed, high-resolution dose fields  $\mathbf{X}$ , enabling fast, resolution-agnostic inference. **c)** Single-step prediction (one-step ahead): Given a sequence of inputs  $\mathbf{Y}_{1:T}$  and spatial queries  $\mathbf{r}$ , a predictor outputs the next dose field  $\mathbf{X}_{t+1}$ . **d)** Full-rollout forecasting (this work): A non-autoregressive operator predicts the entire future sequence  $\mathbf{X}_{1:K}$  from  $(\mathbf{Y}, \mathbf{r})$  in a single pass (solid arrows), supporting stable, long-range, full-field reconstruction.

The collection of dose rates across  $P$  evaluation points forms the dose field  $\mathbf{X} = \{X_1, \dots, X_P\} \in \mathbb{R}^P$ . This defines a latent physical operator  $\mathcal{H}_{\text{phys}} : (\Phi, A, G, h) \rightarrow \mathbf{X}$ . While physically grounded, this forward approach is computationally expensive due to the need for extensive Monte Carlo transport simulations, making it infeasible for real-time global monitoring (Figure 1a).

To overcome the limitations of forward modeling, we formulate an inverse problem that directly maps observable proxies (i.e., neutron counts on the ground) to the desired dose fields. Instead of simulating latent variables like  $\Phi$ , the model learns a spatiotemporal operator  $\mathcal{H}$  that reconstructs the dose field  $\mathbf{X}$  from the observed neutron monitor time series  $\mathbf{Y}$  and a set of spatial query coordinates  $\mathbf{r}$ . We define this learned inverse operator as:

$$\mathbf{X} = \mathcal{H}(\mathbf{Y}, \mathbf{r}) \quad (3)$$

where  $\mathbf{Y} \in \mathbb{R}^{T \times N}$  is the input from the neutron monitors and  $\mathbf{r} \in \mathbb{R}^P$  represents the spatial query locations. This formulation bypasses the explicit simulation of intermediate physical processes, enabling fast, resolution-agnostic reconstruction of the global radiation dose distribution from real-world sensor data (Figure 1b). The neutron counting data used in this study was obtained from the Neutron Monitor Database (NMDB) [34, 35].

Notably, forecasting models that are designed for problems where the input and target fields share a common spatial domain cannot be directly applied to this problem. The problem setup involves a fundamental domain mismatch: sparse, irregularly distributed ground-based measurements as input, versus dense, global radiation dose fields at high altitudes as output. This domain mismatch, combined with the incomplete spatial coverage of the observational network, violates the assumptions of structured, grid-based inputs covering the entire target domain.

In addition, the problem is designed to solve for a sequence-to-sequence solution. In autoregressive schemes, a model iteratively consumes its own predictions as input, which leads to compounding errors over long horizons. In contrast, our non-autoregressive formulation predicts the entire future trajectory in a single pass, thereby mitigating error accumulation (Figure 1d). Namely, we learn an operator  $\mathcal{H}$  that maps an input sequence of sensor observations  $\mathbf{Y} \in \mathbb{R}^{T \times N}$  and a set of spatial query coordinates  $\mathbf{r} \in \mathbb{R}^P$  to the full sequence of future dose fields  $\mathbf{X}_{1:K} \in \mathbb{R}^{P \times K}$ :

$$\mathbf{X}_{1:K} = \mathcal{H}(\mathbf{Y}, \mathbf{r}),$$

where  $K$  denotes the number of leading forecast steps.

The methodology employs an effective dose dataset [36] calculated using EXPACS [37, 38, 39] for an altitude of 10,000 m at a  $1^\circ$  latitude–longitude resolution, replicating environmental conditions relevant to aviation safety and space weather monitoring. The dataset is generated at a daily temporal resolution, providing dose estimates under varying geomagnetic and atmospheric conditions. Following the EXPACS code manual [39], the water fraction parameter was set to 0.15, representing the recommended setting. This dataset is designed to evaluate the model’s ability to reconstruct high-dimensional spatiotemporal fields from sparse measurements, which are characteristic of the complex dynamics of cosmic radiation dose.

The dataset is structured into three primary components to facilitate operator learning. The *Branch Input* consists of time-series measurements of neutron counts derived from a global network of 12 sparse, ground-based neutron monitors. These measurements, spanning the period from 2001 to 2023, serve as indirect proxies for the cosmic radiation field at each time step. Concurrently, the *Trunk Input* provides the spatial query points for field reconstruction, defined by global grid coordinates normalized to the interval  $[0, 1]$  for both latitude and longitude, thereby offering a continuous representation of the spatial domain. The *Target Output*, serves as the ground-truth reference for model evaluation and is composed of the full-field radiation dose rates across the global grid corresponding to each time step.

Data preprocessing involves the construction of input-output pairs using a sliding window approach to capture temporal dependencies. A temporal window of a fixed size,  $T = K = 180$ , is applied to the neutron counts time series, generating sequences of input observations that are paired with the corresponding future radiation dose fields over an identical prediction horizon steps. The dataset is subsequently partitioned into training (45%), validation (10%), and testing (45%) subsets. Crucially, the test set is reserved for evaluating the model’s generalization to unseen temporal regimes. This chronological split preserves temporal continuity, ensuring that the model is assessed under realistic conditions where future states are not available during training. This preprocessing strategy is designed to facilitate robust training and evaluation of the STONe model for its designated tasks of long-term forecasting and spatiotemporal field reconstruction.

## 2.2 DeepONet Framework

The DeepONet is a neural network architecture designed to learn nonlinear operators, which are mappings between infinite-dimensional function spaces,  $\mathcal{G} : \mathcal{I} \rightarrow \mathcal{O}$  [16]. The theoretical foundation for this architecture is the universal approximation theorem for operators, which states that a neural network can approximate any nonlinear continuous operator to arbitrary accuracy [40].

A DeepONet approximates the evaluation of an output function  $\mathcal{G}(\mathbf{u})$  at a specific query location  $\mathbf{r} \in \Omega \subset \mathbb{R}^d$ . The architecture achieves this through two distinct subnetworks. The first is the **Branch Network**, which encodes the input function  $\mathbf{u} \in \mathcal{I}$  by evaluating it at a fixed set of  $m$  sensor locations  $\{\mathbf{x}_j\}_{j=1}^m \subset \Omega$ . This network processes the discrete representation,  $[\mathbf{u}(\mathbf{x}_1), \dots, \mathbf{u}(\mathbf{x}_m)]$ , to produce a latent vector representation  $\mathbf{b}(\mathbf{u}) \in \mathbb{R}^q$ . The second subnetwork is the **Trunk Network**, which encodes the continuous domain of the output function by taking a query coordinate  $\mathbf{r} \in \Omega$  as input and mapping it to a corresponding basis vector  $\mathbf{t}(\mathbf{r}) \in \mathbb{R}^q$ . The operator's output at the location  $\mathbf{r}$  is then approximated by the inner product of the outputs from these two networks, often with an added bias term  $\beta$ :

$$\mathcal{G}_\theta(\mathbf{u})(\mathbf{r}) = \sum_{i=1}^q b_i(\mathbf{u}) t_i(\mathbf{r}) + \beta \approx \mathcal{G}(\mathbf{u})(\mathbf{r}), \quad (4)$$

where  $\theta$  denotes the set of all trainable parameters. This architecture learns separate representations for the input function and the output evaluation coordinates. This separation allows the model to make predictions at any location, independently from the training data's resolution and domain. Consequently, the framework is highly flexible and well-suited for modeling diverse physical systems.

### 2.3 Spatio-Temporal Operator Network (STONe)

To forecast the evolution of high-dimensional spatiotemporal systems, we adapt the S-DeepONet architecture to learn the system's evolution operator. The proposed structure is designed to approximate the mapping  $\mathcal{G}_\theta$  from a history of  $K_{\text{hist}}$  state observations to a sequence of  $K_{\text{fut}}$  future states. The operator maps the time-dependent input history  $\mathbf{u}_{\text{hist}}(t) = \{\mathbf{y}(t-(k-1)\Delta t, \cdot)\}_{k=1}^{K_{\text{hist}}}$  to a multivariate output field  $\mathbf{y}(\mathbf{r}, t_k) \in \mathbb{R}^p$  for a sequence of future times  $t_k = t + k\Delta t$ , where  $p$  is the number of physical quantities of interest, and  $k$  is a future time-step index  $k \in \{1, \dots, K_{\text{fut}}\}$ .

This framing is analogous to data-driven PDE discovery, where sparse identification methods are used to find parsimonious dynamical models from measurement data [15, 14]. In this STONe architecture, the **branch network** processes the input history  $\mathbf{u}_{\text{hist}}$  to produce a set of time-dependent coefficients  $\mathbf{b}(\mathbf{u}_{\text{hist}}) \in \mathbb{R}^q$  that encode the temporal dynamics, while the **trunk network** takes as input a spatial coordinate  $\mathbf{r}$  and a future time-step index  $k$  to output a matrix of spatiotemporal basis functions  $\mathbf{T}(\mathbf{r}) \in \mathbb{R}^{q \times p \times K}$ .

The prediction for the  $p$ -dimensional state vector at location  $\mathbf{r}$  and future time  $t_k$  is synthesized via a matrix-vector product. Specifically, the  $j$ -th component of the predicted state,  $y_j$ , is given by:

$$y_j(\mathbf{r}, t + k\Delta t) = \sum_{i=1}^q b_i(\mathbf{u}_{\text{hist}}) T_{ijk}(\mathbf{r}) + \beta_j, \quad \text{for } j = 1, \dots, p, \text{ and } k = 1, \dots, K_{\text{fut}}, \quad (5)$$

where  $b_i$  is the  $i$ -th element of the branch output,  $T_{ijk}$  is the element of the trunk's output matrix corresponding to the  $i$ -th latent dimension and  $j$ -th output variable at  $k$ -th lead time, and  $\beta_j$  is a learnable bias for the  $j$ -th output channel.

This formulation establishes a parallel with modal decomposition techniques [11, 13]. The branch network learns to compute the optimal temporal coefficients, while the trunk network learns the optimal spatiotemporal basis functions directly from data. This end-to-end learning process bypasses the explicit eigendecompositions of traditional methods and can capture complex, nonlinear relationships. Such a generalization empowers STONe for full-rollout forecasting in non-Markovian regimes, rendering it particularly advantageous for high-dimensional spatiotemporal reconstruction, long-term dynamical forecasting, and multi-physics simulations where capturing memory-dependent evolution is essential.

### 2.4 Model Architecture and Training

The STONe is realized using a modular architecture where the branch and trunk networks function as temporal and spatiotemporal encoders, respectively (Figure 2).

The **branch network** is designed to encode the temporal dependencies within the input history,  $\mathbf{u}_{\text{hist}} \in \mathbb{R}^{K_{\text{hist}} \times N}$ , where  $K_{\text{hist}}$  is the number of historical time steps and  $N$  is the dimension of the state vector at each step (e.g., number of sensors multiplied by the number of channels). Its objective is to map this input sequence to a latent representation of the system's current dynamical state, producing the temporal coefficient vector  $\mathbf{b}(\mathbf{u}_{\text{hist}}) \in \mathbb{R}^q$ . To investigate different temporal feature extraction capabilities, we evaluate several architectures for this network: Gated Recurrent Units (GRUs), Long Short-Term Memory (LSTM) networks, and the Transformer architecture [41, 42, 43]. A standard fully-connected network (FCN) that processes a flattened input vector serves as a baseline [44]. For all configurations, the core architecture consists of three hidden layers, with a latent dimension of  $q = 128$ . For the Transformer, we employ a multi-head attention mechanism with 8 heads to effectively capture complex temporal patterns.

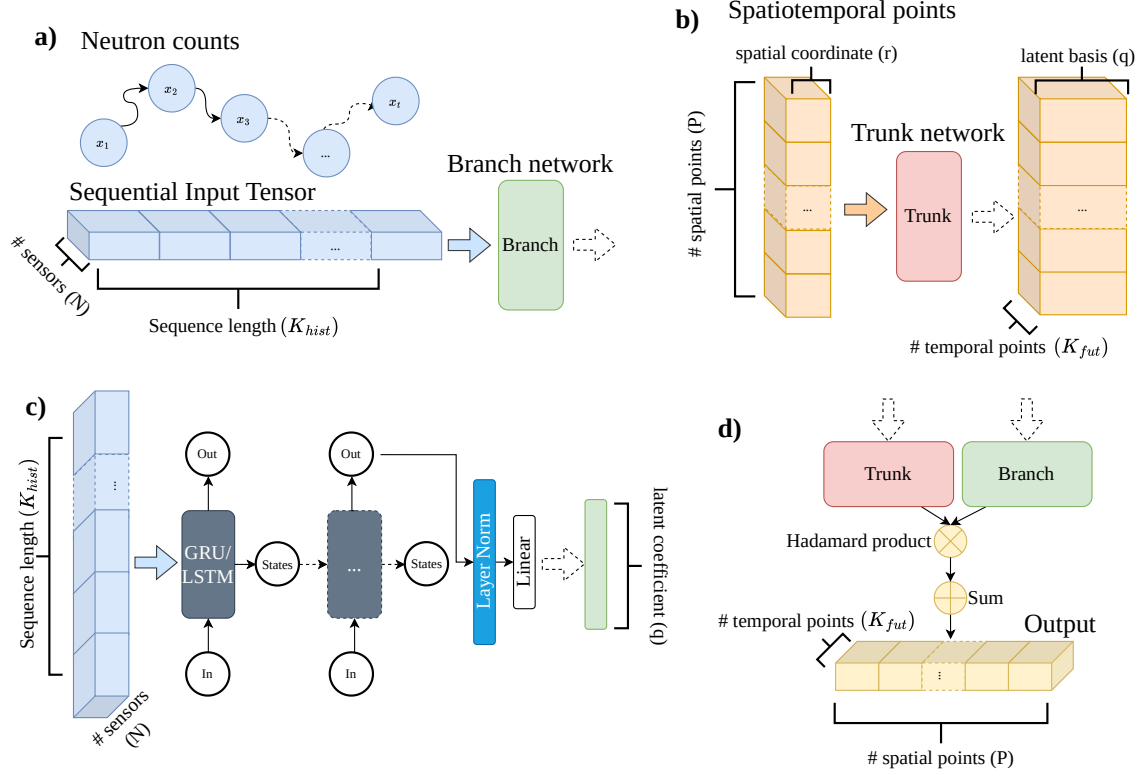


Figure 2: **STONe Architecture for Spatiotemporal Forecasting.** The modular design integrates temporal and spatiotemporal encoders where the branch network captures historical dynamics through sequence processing models, while the trunk network generates coordinate-dependent basis functions. The architecture enables principled forecasting by learning the mapping from sparse sensor histories to dense future field reconstructions. (a) Branch Network Temporal Encoder. The branch network processes sequential sensor input history  $u_{\text{hist}} \in \mathbb{R}^{K_{\text{hist}} \times N}$  through temporal encoders (GRU, LSTM, or Transformer) to extract dynamical state features and produce temporal coefficient vector  $b(u_{\text{hist}}) \in \mathbb{R}^q$ . (b) Trunk Network Spatiotemporal Decoder. The trunk network maps spatiotemporal coordinates ( $r$ ) through fully connected layers to generate basis functions  $T(r) \in \mathbb{R}^{q \times p \times K_{\text{fut}}}$ , representing the evaluation of  $q$  basis functions across  $p$  spatial points and  $K_{\text{fut}}$  future time points. (c) Sequential Data Processing Pipeline. Historical sensor measurements from  $K_{\text{hist}}$  past time steps are fed into the branch network’s temporal encoder, which captures complex temporal dependencies and system dynamics to encode the current dynamical state. (d) Future State Reconstruction (Output). The STONe combines temporal coefficients from the branch network with spatiotemporal basis functions from the trunk network to reconstruct the complete future state sequence over  $K_{\text{fut}}$  time steps through tensor contraction.

The **trunk network** acts as a spatiotemporal decoder, responsible for generating the basis functions upon which the dynamics evolve. It is implemented as a fully connected network with two hidden layers, each containing 128 neurons. This network maps a given spatiotemporal coordinate pair, consisting of a spatial location  $\mathbf{r}$  and a historical time  $k \in K_{hist}$ , to the spatiotemporal basis matrix  $T(\mathbf{r}) \in \mathbb{R}^{q \times p \times K_{fut}}$ . This output represents the evaluation of the  $q$  basis functions for each of the  $p$  specific points in the future time set  $K_{fut}$ .

The model's trainable parameters are optimized by minimizing the mean squared error (MSE) loss function. We employ the Adam optimizer with an initial learning rate of  $1 \times 10^{-3}$ . To dynamically adjust the learning rate, a ReduceLROnPlateau scheduler was used, which reduces the learning rate by a factor of 0.5 if the validation loss does not improve by a threshold of  $1 \times 10^{-4}$  for 5 consecutive epochs, down to a minimum learning rate of  $1 \times 10^{-7}$ . To mitigate overfitting, the training process is regularized using early stopping with a patience of 10 epochs, monitored on a held-out validation set. The model is trained for a maximum of 500 epochs on a high-performance, CUDA-enabled NVIDIA H100 GPU.

## 2.5 Evaluation Metrics

To provide a comprehensive assessment of model performance, we employ a multi-faceted evaluation protocol designed to quantify both predictive accuracy and computational efficiency. The performance of the proposed STONe architectures is systematically compared against a vanilla DeepONet baseline to rigorously evaluate the benefits of the sequential, non-autoregressive formulation.

The primary measure of forecasting accuracy is the relative L2 error ( $\epsilon$ ), computed over the test dataset. This metric quantifies the model's ability to reconstruct the full spatiotemporal radiation field,  $\mathbf{y}(\mathbf{r}, t)$ , by comparing the predicted field,  $\hat{\mathbf{y}}(\mathbf{r}, t)$ , to the ground-truth reference from the physics-based simulations. The error is defined as:

$$\epsilon = \frac{\|\mathbf{y} - \hat{\mathbf{y}}\|_{L_2}}{\|\mathbf{y}\|_{L_2}} \quad (6)$$

where  $\|\cdot\|_{L_2}$  denotes the standard L2 norm computed across all spatial points and future time steps in the prediction horizon. To diagnose performance degradation over time, this metric is evaluated at each future lead time,  $k \in \{1, \dots, K_{fut}\}$ , providing insight into the model's error growth characteristics.

Additionally, the Mean Absolute Error (MAE) and Mean Absolute Percentage Error (MAPE) are reported to assess the preservation of spatial structures crucial for identifying high-risk radiation zones and capturing the magnitude of errors in visualized model performances. The MAE is defined as:

$$\text{MAE} = \frac{1}{n} \sum_{i=1}^n |y_i - \hat{y}_i| \quad (7)$$

where  $n$  represents the total number of spatiotemporal points. The MAPE provides a normalized perspective on prediction accuracy:

$$\text{MAPE} = \frac{1}{n} \sum_{i=1}^n \left| \frac{y_i - \hat{y}_i}{y_i} \right| \times 100\% \quad (8)$$

These complementary metrics enable comprehensive evaluation of both absolute and relative prediction errors across the spatiotemporal domain.

Beyond accuracy, the practical viability of the model for real-time applications is assessed through its efficiency. We evaluate the computational cost by measuring the total number of trainable parameters, which reflects the model's memory footprint, the computation required for its training, and the average inference time needed to generate a full-field forecast, all of which are critical for operational deployment.

This dual-focus evaluation ensures a holistic comparison, highlighting the STONe's suitability for producing high-fidelity field reconstructions in real-time, sparse-data, domain-mismatching regimes.

In addition to these quantitative metrics, we conduct a qualitative assessment to evaluate the model's ability to reproduce the physical characteristics of the radiation fields. While aggregate error metrics provide a global measure of accuracy, they can obscure localized discrepancies or a model's failure to capture critical spatial structures, such as the sharp gradients and peak intensities of high-risk radiation zones. Therefore, we perform a side-by-side visual comparison of the predicted fields against the ground-truth simulations at multiple forecast lead times. This visual analysis is crucial for verifying the structural fidelity and physical plausibility of the forecasts, ensuring that the model's predictions are not only numerically accurate but also qualitatively correct. This approach provides a more holistic understanding of model performance, complementing the quantitative results.

### 3 Results

The performance of the STONe was evaluated using four distinct temporal encoders for the branch network: FCN, LSTM, GRU, and Transformer. This section presents a comparative analysis of their forecasting accuracy and computational efficiency.

#### 3.1 Qualitative Results

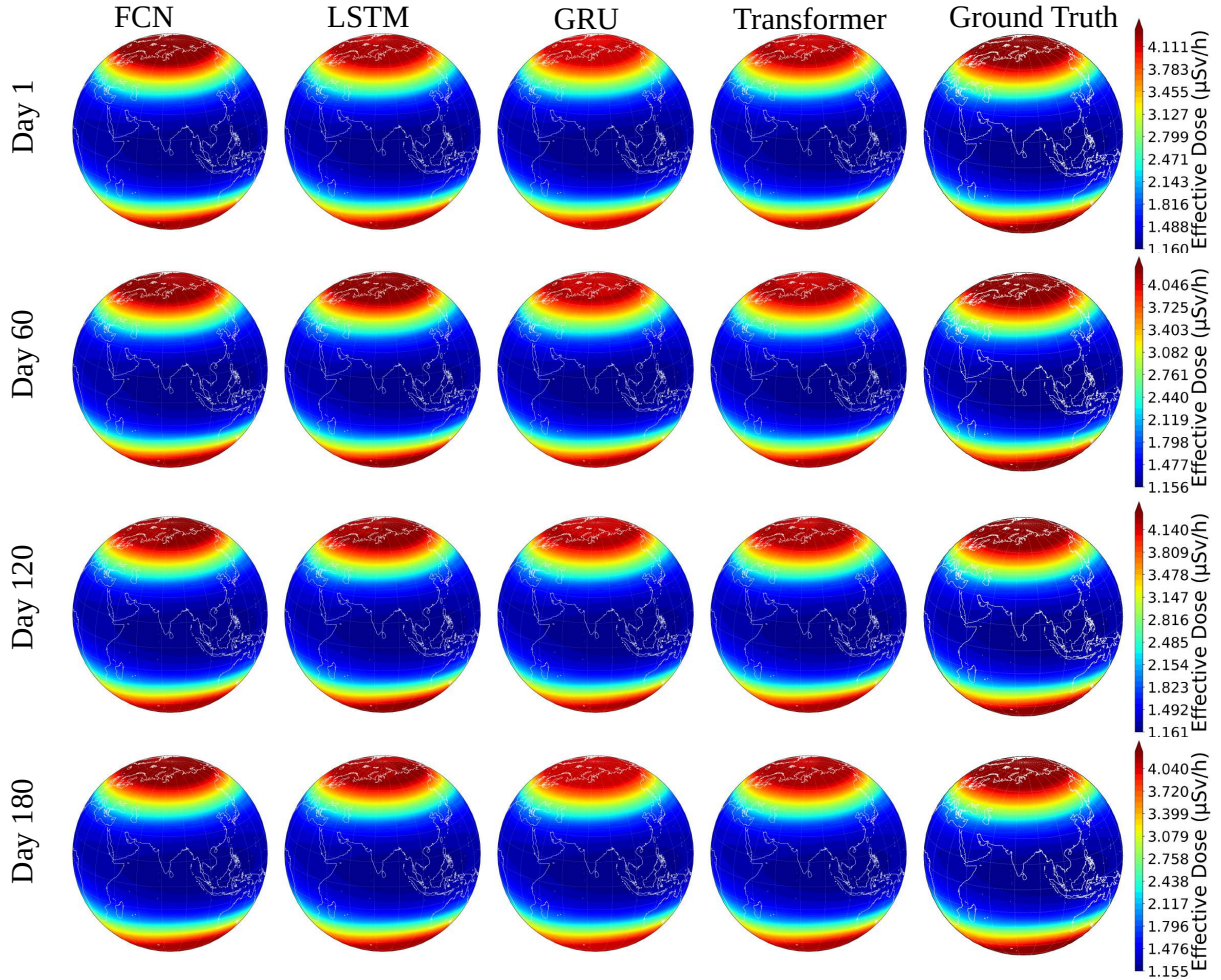


Figure 3: **Qualitative effective dose comparison of multi-day forecasting performance for the four STONe branch architectures against ground truth.** Each row corresponds to a different forecast lead time: Day 1 (row 1), Day 60 (row 2), Day 120 (row 3), and Day 180 (row 4). The last column shows the ground truth dose field, followed by predictions from each model architecture.

Figure 3 provides a qualitative assessment of the models' spatiotemporal reconstruction capabilities at different forecast horizons (Days 1, 60, 120, and 180). The visualizations correspond to the same representative sample from the test set, allowing for direct comparison of how each model captures the evolution of the cosmic radiation field.

For effective dose forecasting, all models demonstrate competent performance, producing forecasts that are visually almost indistinguishable from the ground truth. As shown in Figure 3, this demonstrates the strength of full-field reconstruction using STONe structures, capturing the location, intensity, and fine-grained spatial features of the primary radiation zones. The STONe variants incorporating sequential encoders (LSTM, GRU, and Transformer) and FCN encoder yield high-fidelity predictions, though with marginally different quantitative errors (Table 1) and subtle visual discrepancies compared to the ground truth reconstruction.

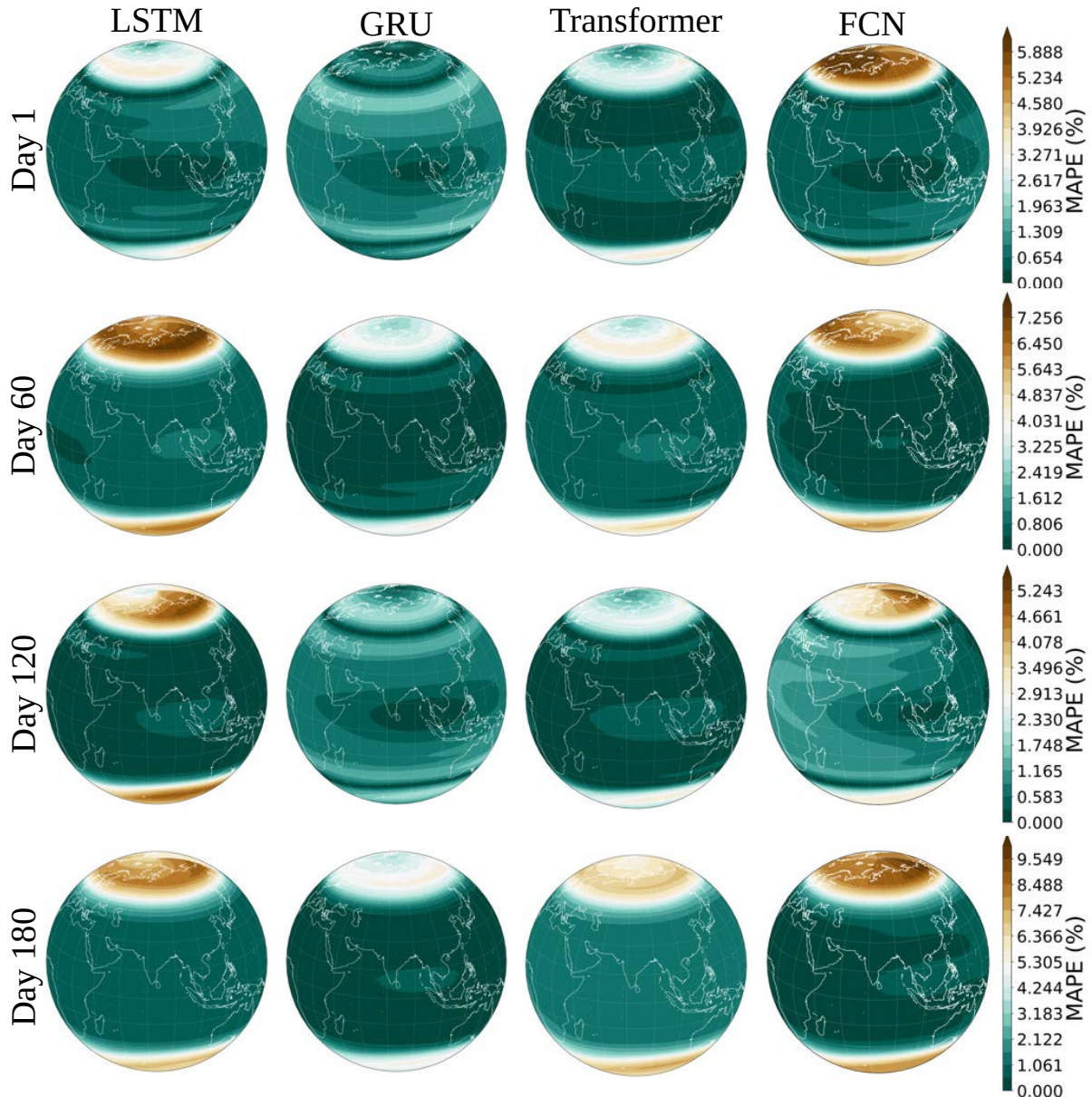
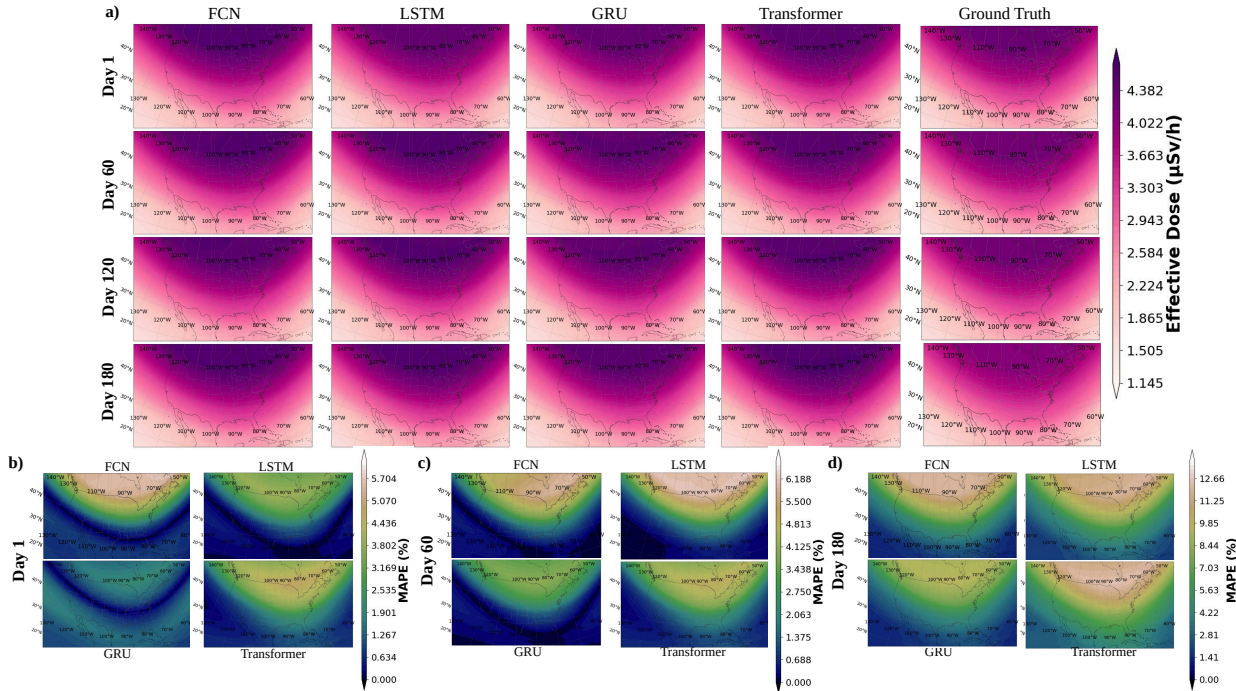


Figure 4: **Mean Absolute Percentage Error (MAPE) comparison of multi-day forecasting performance for the four STONe branch architectures against ground truth.** Each row corresponds to a different forecast lead time: Day 1 (row 1), Day 60 (row 2), Day 120 (row 3), and Day 180 (row 4). The results show the MAPE against the ground truth at each forecasting lead time.

Figure 4 provides insights to evaluate the superiority of variants more rigorously through visual analysis. Each row represents the forecasting results for lead times of 1, 60, 120, and 180 days, compared against the ground truth, with the MAPE calculated at each spatiotemporal point.

For near-term forecasting at Day 1, all S-DeepONet variants demonstrate superior performance compared to the vanilla DeepONet. As the forecast horizon extends to Day 60, differences in performance become more apparent. The FCN and LSTM models begin to lose some finer spatial details, resulting in slightly blurred reconstructions in extreme regions near the poles. As the forecast horizon extends to Days 120 and 180, the GRU and Transformer models maintain higher fidelity, preserving sharp gradients and complex shapes of the radiation patterns more effectively.

At the longest lead time (Day 180), the differences are most pronounced. The FCN’s predictions, while still capturing the general location of low-intensity regions near the equator, suffer from significant oversmoothing. The GRU and Transformer models demonstrate superior performance, retaining a high degree of structural similarity to the ground truth. This visual evidence corroborates the quantitative findings, confirming that while all models are effective for short-term prediction, architectures designed to explicitly model temporal sequences (GRU and Transformer) are more robust for long-range spatiotemporal forecasting.



**Figure 5: Case Study: Radiation Dose Forecasting for the North American Region.** This figure presents a detailed performance evaluation of the four STONe branch architectures for a 180-day forecast. **(a)** Qualitative comparison of the predicted effective dose fields from the FCN, LSTM, GRU, and Transformer models against the ground truth (GT) at forecast lead times of 1, 60, 120, and 180 days. All plots in this panel share a color scale. **(b-d)** Quantitative error analysis showing the Mean Absolute Percentage Error (MAPE) for each architecture at **(b)** Day 1, **(c)** Day 60, and **(d)** Day 180. The color scales in the error plots are independent for each lead time to better visualize the relative performance differences between models.

To assess the operational utility of the proposed framework, we conduct a detailed case study focusing on the North American region, which currently experiences the highest volume of global air traffic. Figure 5 presents a comprehensive evaluation of the four STONe branch architectures on a representative test sequence independent from the global analyses presented in previous sections.

The qualitative results (Fig. 5a) demonstrate that all four architectures (FCN, LSTM, GRU, and Transformer) successfully reconstruct the primary spatial features of the effective dose field across the 180-day forecast horizon. The characteristic latitudinal gradient of cosmic radiation is well-captured, and the predicted fields remain physically plausible and visually coherent even at extended lead times, validating the overall STONe framework for regional forecasting.

A quantitative analysis of the prediction error, however, reveals significant performance differences between the architectures. Figures 5b–d show the Mean Absolute Percentage Error (MAPE) at forecast days 1, 60, and 180. While all models perform well initially with low error across the domain (Fig. 5b), their long-term stability diverges considerably. By Day 180 (Fig. 5d), the benefits of sequential encoders become apparent. The GRU variant maintained significantly lower error, representing superior stability for long-range forecasting.

Notably, in the high-latitude northern regions, where the radiation dose is most intense and poses the greatest health risk, the GRU variant demonstrates exceptional robustness. At the 180-day lead time, it is the only architecture to maintain a MAPE below 10% in these critical areas. In contrast, the FCN, LSTM, and Transformer models exhibit significantly higher errors, exceeding 10% MAPE, indicating a degradation in their predictive fidelity. This high-resolution regional case study support the findings from our global analysis: while all branch structures capture the global pattern of the radiation dose, the GRU-based STONe presents the strongest and most stable performance, making it the most promising candidate for reliable, long-horizon operational forecasting.

### 3.2 Quantitative Forecasting Accuracy

To complement the qualitative evaluation, a comprehensive quantitative analysis was conducted to evaluate the forecasting accuracy of the four model architectures. Performance was assessed using three standard metrics: relative L2 error, RMSE, and MAE over the unseen test dataset. The results are presented both at discrete intervals in Table 1 and as a continuous error profile in the heatmap in Figure 6. Across all evaluations, the GRU-based architecture consistently emerges as the most accurate and stable model.

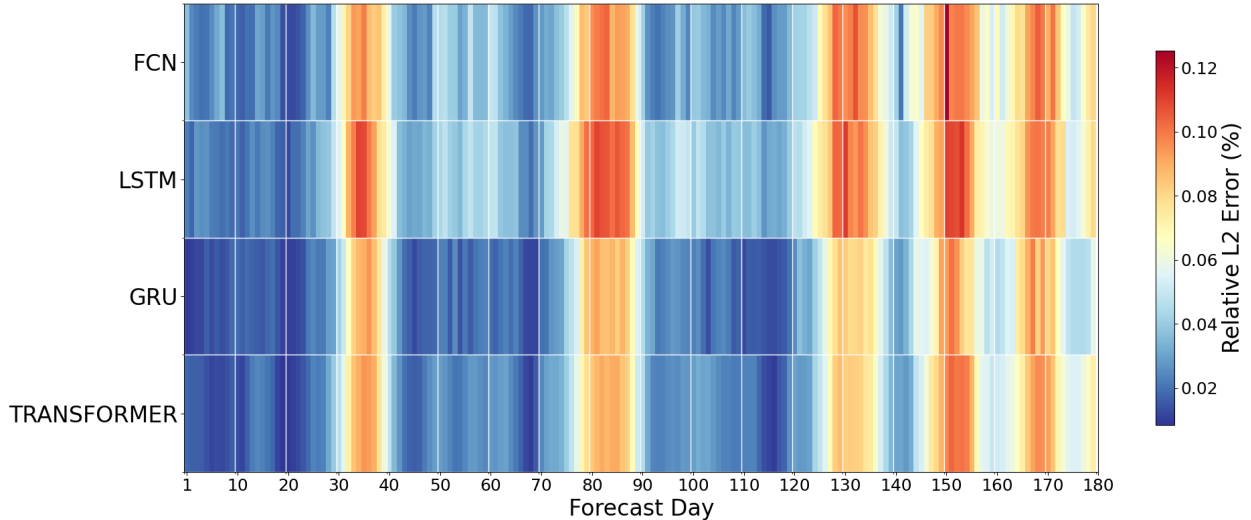


**Figure 6: Relative L2 error heatmap across STONe branch architectures.** Each row represents the average relative L2 error for each forecast day from 1 to 180. Lower errors (closer to 0) are represented in darker blue, while higher errors (up to 0.12) are shown in darker red. The GRU model consistently demonstrates the lowest error rates across the entire forecasting horizon.

Figure 6 presents a visual representation of the performance across the 180-day forecasting lead time by evaluating each model on the unseen test set and computing the average relative L2 error for each lead time. The GRU model demonstrates a distinct advantage across all time horizons, achieving the lowest error rates in the most challenging forecasting regions where other models exhibit poor performance (represented by dark red regions in the heatmap). Furthermore, the GRU model maintains superior performance in easily forecastable regions where other models also perform well, as evidenced by the darker blue coloring in those areas, indicating lower Relative L2 Error. These results show that the GRU model not only generalizes better in diverse forecasting conditions but also exhibits superior specialization capabilities. The superior performance in challenging regions suggests that the GRU model produces more stable and consistent forecasts, resulting in reduced error accumulation in difficult-to-predict scenarios.

A clear pattern of error-prone regions and error accumulation is observable across all models. This behavior, where error metrics generally increase with forecast lead time, is characteristic of multi-step forecasting models, as small initial inaccuracies propagate and amplify throughout the prediction sequence. The GRU and Transformer architectures experience the least error accumulation, maintaining moderate performance levels toward the end of the 180-day forecasting period. However, the global trend of elevated errors in specific temporal regions persists across all models.

Table 1: **Performance comparison of forecasting models across different lead times.** The table provides a comprehensive comparison of the Relative L2 Error (%), Root Mean Squared Error (RMSE), and Mean Absolute Error (MAE) for each of the four STONe branch architectures across the 180-day forecasting lead time at 30-day intervals. The best performance for each metric at a given forecast day is highlighted in bold.

Forecast Lead Time (Day)	Model	Relative $L_2$ Error (%)	RMSE	MAE
1	FCN	0.0370	0.1214	0.0876
	LSTM	0.0223	0.0732	0.0529
	GRU	<b>0.0096</b>	<b>0.0316</b>	<b>0.0261</b>
	Transformer	0.0178	0.0583	0.0412
30	FCN	0.0463	0.1481	0.1069
	LSTM	0.0491	0.1570	0.1156
	GRU	<b>0.0295</b>	<b>0.0939</b>	<b>0.0695</b>
	Transformer	0.0395	0.1262	0.0962
60	FCN	0.0354	0.1155	0.0825
	LSTM	0.0445	0.1450	0.1039
	GRU	<b>0.0234</b>	<b>0.0763</b>	<b>0.0552</b>
	Transformer	0.0241	0.0786	0.0570
90	FCN	0.0573	0.1800	0.1362
	LSTM	0.0673	0.2119	0.1619
	GRU	0.0546	0.1714	0.1306
	Transformer	<b>0.0513</b>	<b>0.1613</b>	<b>0.1252</b>
120	FCN	0.0351	0.1146	0.0832
	LSTM	0.0398	0.1300	0.0941
	GRU	<b>0.0197</b>	<b>0.0643</b>	<b>0.0467</b>
	Transformer	0.0259	0.0845	0.0627
150	FCN	0.0968	0.3005	0.2239
	LSTM	0.0918	0.2849	0.2214
	GRU	0.0916	0.2842	0.2209
	Transformer	<b>0.0885</b>	<b>0.2747</b>	<b>0.2181</b>
180	FCN	0.0808	0.2559	0.1873
	LSTM	0.0799	0.2529	0.1921
	GRU	<b>0.0576</b>	<b>0.1820</b>	<b>0.1368</b>
	Transformer	0.0731	0.2313	0.1825
Avg.	FCN	0.0523	0.1656	0.1235
	LSTM	0.0566	0.1794	0.1348
	GRU	<b>0.0415</b>	<b>0.1311</b>	<b>0.0995</b>
	Transformer	0.0440	0.1389	0.1073

Additionally, forecasts at later stages suffer more significantly from accumulated errors, as the fundamental limitation of decreasing information availability over extended horizons remains unresolved. Collectively, all performance metrics suggest that the GRU architecture possesses superior capacity for retaining long-term dependencies compared to other architectures in this cosmic muon operator learning scenario.

Table 1 provides a detailed quantitative breakdown of the models’ performance at discrete intervals, reinforcing the findings from the heatmap. The GRU architecture consistently demonstrates superior performance, achieving the lowest average error across all metrics: Relative L2 Error (0.0415), RMSE (0.1311), and MAE (0.0995). The Transformer model is a strong competitor, securing the second-best average performance and even outperforming the GRU at specific intermediate forecast horizons (Day 90 and 150), which suggests a particular strength in capturing mid-range dependencies. In contrast, the FCN and LSTM models consistently lag behind, exhibiting higher error rates that indicate a greater difficulty in modeling the complex, long-term temporal patterns of the data. These quantitative results confirm that the GRU’s robust performance across the majority of the forecast lead times establishes it as the most stable and accurate architecture for this task.

### 3.3 Computational Efficiency

Table 2: Computational performance and training characteristics of the different branch architectures. Inference time is the average time to generate a single 180-day forecast sequence.

Branch Architecture	Parameters (M)	Train Time (min/Epoch)	Train Epochs to Converge	Inference Time (ms)
FCN	3.1028	5.8368	12	0.0420
GRU	3.3741	5.7769	15	0.0480
LSTM	3.4913	5.8026	12	0.0600
Transformer	5.9889	5.8225	35	0.0450

The computational performance and training characteristics of each model architecture are detailed in Table 2. The FCN is the most compact model, while the Transformer has the largest parameter count due to its multi-head attention mechanisms. Despite these differences in size, all architectures exhibit sub-millisecond inference times for a full 180-day forecast. The Transformer’s highly parallelizable architecture allows its inference speed to be competitive with the smaller recurrent models (GRU, LSTM), highlighting a non-linear relationship between parameter count and inference latency.

Regarding training, the time per epoch was comparable across all architectures, averaging just under 6 minutes. However, the number of epochs required for convergence, as determined by our early stopping criteria, varied significantly. The Transformer model, with its larger parameter space, required more than double the training epochs of the recurrent models to converge. All models were trained on a single NVIDIA H200 GPU, with a maximum recorded memory usage of 26,636 MiB during the training process. Performance benchmarks for inference were conducted on the same hardware, where the reported time is an average of 100 runs over the 365-day test dataset.

#### Key Findings from STONe Evaluation

- **Solves a Challenging Inverse Problem:** The STONe framework successfully forecasts dense, global atmospheric radiation fields from sparse, irregular ground-based measurements, overcoming the input-output domain mismatch that limits many state-of-the-art models.
- **Superior GRU-based Performance:** The GRU architecture is the top-performing model, achieving the lowest average error metrics across the 180-day forecast (Relative L2 Error of 0.0415, RMSE of 0.1311, and MAE of 0.0995).
- **Robust Long-Term Stability:** The GRU and Transformer architectures demonstrate high resilience to error accumulation, ensuring stable and reliable performance across the entire forecasting horizon, unlike less complex models.
- **Real-Time Operational Viability:** All tested architectures maintain inference speeds suitable for real-time deployment, bridging the gap between high-fidelity forecasting and practical operational requirements.

## 4 Discussion

We have presented STONe, a non-autoregressive neural operator framework capable of long-horizon, sparse-to-dense forecasting in a cross-domain setting. Our results demonstrate that learning a direct sequence-to-sequence operator is not only feasible but also robust against the error accumulation that limits iterative methods.

Leading deep learning models for weather and climate forecasting, such as NeuralGCM [7], Pangu-Weather [4], GraphCast [6], GenCast [8], and FourCastNet [5], have achieved remarkable success in their respective domains. These models leverage sophisticated architectures: hybrid NWP-MLWP model, 3D Earth-specific transformer, GNNs and Vision Transformers with FNOs, respectively, to capture complex spatial dependencies and scale to high-resolution global data.

Table 3: Comparison of **STONe (this paper)** with state-of-the-art data-driven weather forecasting models. The table highlights fundamental differences in problem formulation, methodology, and scale. Note that a direct numerical comparison of forecast accuracy is not applicable due to the disparate nature of the problems being solved (e.g., sparse-to-dense vs. dense-to-dense).

Metrics	STONe	NeuralGCM	GraphCast	Pangu-Weather	FourCastNet
<b>Purpose</b>	Sparse-to-dense cross-domain forecasting.	Hybrid physics-ML weather climate simulation.	Dense-to-dense, medium-range weather forecasting.	Dense-to-dense, medium-range weather forecasting.	Dense-to-dense, medium-range weather forecasting.
<b>Model Size</b>	3.1M – 6.0M parameters.	11.5M – 31.1M parameters + numerical solver.	36.7M parameters.	64M parameters per base model (x4).	Not specified.
<b>Training Data</b>	NMDB (2001–2023).	ERA5 reanalysis (1979–2019).	ERA5 reanalysis (1979–2017).	ERA5 reanalysis (1979–2017).	ERA5 reanalysis (1979–2015).
<b>Training Time</b>	1 – 2 hours on a single H200 GPU.	1 day – 3 weeks on 16–256 TPUs.	4 weeks on 32 Cloud TPU v4 devices.	16 days on 192 V100 GPUs (per model).	16 hours on 64 A100 GPUs.
<b>Grid Resolution</b>	<i>Input:</i> 12 points. <i>Output:</i> $1^\circ \times 1^\circ$ dense grid.	$0.7^\circ, 1.4^\circ, 2.8^\circ$ dense grids.	$0.25^\circ \times 0.25^\circ$ dense grid.	$0.25^\circ \times 0.25^\circ$ dense grid.	$0.25^\circ \times 0.25^\circ$ dense grid.
<b>Forecasting Horizon</b>	180 days (180 steps at 1-day increments)	$\leq 15$ days (360 steps at 1-hour increments)	10 days (40 steps at 6-hour increments)	$\leq 7$ days (28 steps at 6-hour increments)	$\leq 8$ days (32 steps at 6-hour increments)
<b>Input Variables</b>	180 time steps of 12 sensor variables.	9 atmospheric variables + extra features	2 time steps of 227 variables	69 atmospheric variables	20 atmospheric variables
<b>Output Variables</b>	180 time steps of 1 radiation dose state.	9 atmospheric states.	227 atmospheric states.	69 atmospheric states.	20 atmospheric states.

However, these models employ an architectural assumption that field-to-field prediction on structured, gridded data is feasible. They operate autoregressively, where the output field at one time step becomes the input field for the next. This paradigm is fundamentally incompatible with the problem addressed in this work, where the input consists of a sparse time series from a few point sensors, and the output is a dense, high-resolution spatial field representing a different physical quantity. This **domain mismatch** makes the direct application of such models impossible (See Table 3).

One could hypothetically adapt existing field-to-field models by creating a multi-stage pipeline: first, an independently trained encoder would map the sparse sensor data to the target field, which would then be fed into an autoregressive forecasting model. However, this approach introduces significant practical challenges. The initial encoder, tasked with reconstructing a dense field from a sparse history, would introduce its own layer of uncertainty. The subsequent forecasting model would then compound not only its own predictive errors at each step but also this initial encoding error. This decoupled learning process adds complexity and potential for information loss. STONe’s end-to-end framework elegantly avoids these issues by learning the cross-domain mapping implicitly within a single, unified operator.

An alternative pipeline could first perform autoregressive forecasting entirely within the sparse sensor domain. In this hypothetical setup, a recurrent or attention-based model would predict future neutron monitor readings from their own history (sensor-to-sensor). Subsequently, at each forecasting time step, a static, independently trained decoder

would map the predicted sensor values to the dense, high-altitude radiation field. However, this decoupled framework introduces critical flaws. The static decoder, which learns a stateless mapping from instantaneous sensor values to the full field, discards the system’s temporal memory which is a physically naive assumption that ignores how the global radiation environment evolves as an integrated function of its history. In contrast, STONe’s end-to-end, sequence-to-sequence operator architecture inherently addresses these limitations. The branch network is trained to extract a holistic representation of the entire input history, which is then used by the trunk network to generate the full future spatiotemporal field in a single forward pass, thereby avoiding both decoupled stages.

The challenge of forecasting a physical field from limited, indirect, or cross-domain observational data is ubiquitous across scientific disciplines; from estimating temperature distribution inside a nuclear reactor using boundary sensors to modeling subsurface fluid flow from sparse well measurements. The proposed STONe framework provides a powerful and generalizable paradigm for these problems.

Our results further demonstrate a clear relationship between branch network structures and forecasting performance across different temporal horizons. For short-term predictions (Day 1), the simpler FCN-based DeepONet achieved comparable performance to more sophisticated architectures. This suggests that for immediate forecasting, a direct nonlinear mapping of recent historical states captures the most salient predictive information, and the additional complexity of recurrent or attention-based encoders provides minimal benefit. However, as the forecast horizon extends, the performance dynamics shift dramatically. For long-range forecasting (Day 180), the GRU architecture emerged as the most accurate model, demonstrating the critical importance of memory-enabled architectures for extended temporal dependencies. This finding supports the hypothesis that sequential architectures are better equipped to capture the cyclical and mean-reverting patterns inherent in cosmic radiation dynamics, thereby mitigating unbounded error growth and yielding superior long-range performance.

From a computational efficiency perspective, all tested architectures proved suitable for real-time applications. Despite the Transformer having over ten times the parameters of the FCN, inference speeds remained nearly identical on the tested hardware (Nvidia H200 GPU). This performance parity indicates that for the operational batch sizes employed, the primary computational bottleneck lies in data handling and memory transfer rather than the model’s forward pass complexity. This efficiency profile confirms the practical viability of deploying even the most parameter-rich STONe variants in time-critical digital twin systems where rapid response is essential.

## Limitations and Outlook

While STONe provides a robust and practical framework for non-autoregressive, sparse-to-dense forecasting, several open challenges remain for future progress.

First, the current STONe implementation is deterministic. For safety-critical applications like aviation, quantifying predictive uncertainty is paramount to risk assessment and decision-making. Future work should integrate probabilistic forecasting capabilities. This could be achieved through deep ensembling, applying Monte Carlo dropout to approximate Bayesian inference, or by adapting STONe into a generative framework, such as a diffusion model, to produce a distribution of possible future radiation fields.

Second, the model faces a scalability limitation regarding memory consumption. The trunk network’s output dimension scales linearly with the number of forecast steps, which can become a bottleneck for predictions over extremely long horizons or at finer spatiotemporal resolutions. Future research could explore more memory-efficient trunk representations, such as using implicit neural representations for the time coordinate or learning a continuous-time evolution operator within the latent space that can be queried at arbitrary future times.

Third, while STONe demonstrates strong performance within the training distribution, its generalization to rare, extreme space weather events (e.g., Carrington-level solar storms) not seen in the historical data remains an open question. Enhancing robustness for out-of-distribution events is a critical next step for operational deployment. This could be achieved by incorporating known physical constraints into the loss function or by augmenting the training dataset with high-fidelity simulations of extreme scenarios.

Fourth, a deeper understanding of the model’s learned representations could yield valuable physical insights. Future work could dissect the learned spatiotemporal dynamics. For instance, analyzing the activation patterns in the GRU’s hidden state could reveal how the model processes historical solar events, while decomposing the trunk network’s basis functions could illuminate the dominant spatial modes of atmospheric radiation transport that it has discovered from data.

By surfacing these challenges, we present STONe as a foundational contribution rather than a final solution. Addressing these limitations will expand its applicability, deepen its reliability, and accelerate the adoption of neural operators as practical, trustworthy tools for forecasting complex physical systems from sparse, real-world sensor data.

## Conclusion and Future Work

The Spatio-Temporal Operator Network (STONe) establishes a new class of neural operators capable of learning stable, cross-domain mappings between physically distinct manifolds. By formulating a non-autoregressive, sequence-to-sequence operator, STONe overcomes two long-standing challenges in scientific forecasting: **domain mismatch** between sensing and prediction spaces, and **error accumulation** in autoregressive inference. This formulation redefines operator learning as a framework for *functional inference across unobservable physical regimes*, extending its scope far beyond radiation modeling to encompass a wide range of inverse and partially observable systems.

**Key findings** from this work are threefold. First, STONe demonstrates that non-autoregressive operator formulations can achieve long-horizon stability without iterative feedback, a capability previously unattainable in operator learning. Second, recurrent and attention-based temporal encoders significantly outperform feedforward architectures in both accuracy and temporal generalization, establishing the importance of sequential modeling in functional operator design. Third, the framework achieves real-time inference at sub-millisecond latency while reconstructing high-resolution radiation dose fields from sparse neutron measurements, marking the first practical realization of cross-domain operator learning for an operational scientific forecasting task.

More broadly, STONe provides a methodological foundation for next-generation **digital twin systems** that combine learned operators with physical models to enable predictive monitoring, anomaly detection, and control in safety-critical domains. For radiation exposure applications, this translates directly into enhanced decision-making for aviation route optimization and space mission planning. Future work will focus on extending STONe to coupled multi-physics systems, developing memory-efficient trunk architectures for longer temporal horizons and higher spatial resolution, and incorporating uncertainty quantification to ensure physically consistent and interpretable operator learning at scale.

### Key Conclusions

- **Solves a Critical Inverse Problem:** STONe successfully forecasts comprehensive radiation fields from sparse, ground-based sensor data, overcoming the domain-mismatch and error-accumulation issues.
- **Bypasses Field-to-Field Architectural Constraints:** Unlike leading autoregressive models, which are constrained to field-to-field predictions on a shared domain, STONe’s operator design directly maps sparse time-series inputs to a dense output field. This avoids the fundamental architectural mismatch that makes other models unsuitable for this class of inverse problem.
- **Ensures Long-Range Stability via Direct Forecasting:** The non-autoregressive framework generates the entire 180-day forecast in a single pass. This direct sequence-to-sequence prediction prevents the cumulative error propagation that fundamentally limits the long-range stability of iterative, autoregressive forecasting schemes.
- **Pathways for Future Research:** Key directions include integrating uncertainty quantification to provide probabilistic forecasts; addressing memory scalability for longer-term predictions through more efficient trunk architectures; enhancing generalization to extreme, out-of-distribution events; and extending the framework to multi-physics systems where coupled dynamics introduce additional complexity.

## Acknowledgments

This research is being performed using funding received from the DOE Office of Nuclear Energy’s Nuclear Energy University Program (NEUP). Award DOE DE-NE0009076.

This work leveraged Delta and DeltaAI advanced computing and data resources, funded by the National Science Foundation (awards OAC <2005572 and OAC <2320345) and the State of Illinois. Delta and DeltaAI are joint initiatives of the University of Illinois Urbana-Champaign and NCSA.

We acknowledge the NMDB database [www.nmdb.eu](http://www.nmdb.eu), founded under the European Union’s FP7 programme (contract no. 213007) for providing data. Additionally, we express our gratitude to the institutions and observatories that maintain

and operate the individual neutron monitor stations, whose invaluable contributions made this work possible. Athens neutron monitor data were kindly provided by the Physics Department of the National and Kapodistrian University of Athens. Jungfraujoch neutron monitor data were made available by the Physikalisches Institut, University of Bern, Switzerland. Newark/Swarthmore, Fort Smith, Inuvik, Nain, and Thule neutron monitor data were obtained from the University of Delaware Department of Physics and Astronomy and the Bartol Research Institute. Kerguelen and Terre Adelie neutron monitor data were provided by Observatoire de Paris and the French Polar Institute (IPEV), France. Oulu and Dome C neutron monitor data were obtained from the Sodankylä Geophysical Observatory, University of Oulu, Finland, with support from the French-Italian Concordia Station (IPEV program n903 and PNRA Project LTCPAA PNRA14-00091). Apatity neutron monitor data were provided by the Polar Geophysical Institute of the Russian Academy of Sciences. South Pole neutron monitor data were supplied by the University of Wisconsin, River Falls.

## References

- [1] Alice J Sigurdson and Elaine Ron. Cosmic radiation exposure and cancer risk among flight crew. *Cancer investigation*, 22(5):743–761, 2004.
- [2] Danielle Silverman and Mark Gendreau. Medical issues associated with commercial flights. *The Lancet*, 373(9680):2067–2077, 2009.
- [3] Robert J Barish. In-flight radiation exposure during pregnancy. *Obstetrics & Gynecology*, 104(3):630, 2004.
- [4] Kaifeng Bi, Lingxi Xie, Hengheng Zhang, Xin Chen, Xiaotao Gu, and Qi Tian. Accurate medium-range global weather forecasting with 3d neural networks. *Nature*, 619(7970):533–538, 2023.
- [5] Jaideep Pathak, Shashank Subramanian, Peter Harrington, Sanjeev Raja, Ashesh Chattopadhyay, Morteza Mardani, Thorsten Kurth, David Hall, Zongyi Li, Kamyar Azizzadenesheli, et al. Fourcastnet: A global data-driven high-resolution weather model using adaptive fourier neural operators. *arXiv preprint arXiv:2202.11214*, 2022.
- [6] Remi Lam, Alvaro Sanchez-Gonzalez, Matthew Willson, Peter Wirnsberger, Meire Fortunato, Ferran Alet, Suman Ravuri, Timo Ewalds, Zach Eaton-Rosen, Weihua Hu, et al. Learning skillful medium-range global weather forecasting. *Science*, 382(6677):1416–1421, 2023.
- [7] Dmitrii Kochkov, Janni Yuval, Ian Langmore, Peter Norgaard, Jamie Smith, Griffin Mooers, Milan Klöwer, James Lottes, Stephan Rasp, Peter Düben, et al. Neural general circulation models for weather and climate. *Nature*, 632(8027):1060–1066, 2024.
- [8] Ilan Price, Alvaro Sanchez-Gonzalez, Ferran Alet, Tom R Andersson, Andrew El-Kadi, Dominic Masters, Timo Ewalds, Jacklynn Stott, Shakir Mohamed, Peter Battaglia, et al. Probabilistic weather forecasting with machine learning. *Nature*, 637(8044):84–90, 2025.
- [9] Tim Palmer. The ecmwf ensemble prediction system: Looking back (more than) 25 years and projecting forward 25 years. *Quarterly Journal of the Royal Meteorological Society*, 145:12–24, 2019.
- [10] Ilya G Usoskin, Agnieszka Gil, Gennady A Kovaltsov, Alexander L Mishev, and Vladimir V Mikhailov. Heliospheric modulation of cosmic rays during the neutron monitor era: Calibration using pamela data for 2006–2010. *Journal of Geophysical Research: Space Physics*, 122(4):3875–3887, 2017.
- [11] Peter J Schmid. Dynamic mode decomposition of numerical and experimental data. *Journal of fluid mechanics*, 656:5–28, 2010.
- [12] Jonathan H Tu. *Dynamic mode decomposition: Theory and applications*. PhD thesis, Princeton University, 2013.
- [13] Steven L Brunton and J Nathan Kutz. *Data-driven science and engineering: Machine learning, dynamical systems, and control*. Cambridge University Press, 2022.
- [14] Steven L Brunton, Joshua L Proctor, and J Nathan Kutz. Discovering governing equations from data by sparse identification of nonlinear dynamical systems. *Proceedings of the national academy of sciences*, 113(15):3932–3937, 2016.
- [15] Samuel H Rudy, Steven L Brunton, Joshua L Proctor, and J Nathan Kutz. Data-driven discovery of partial differential equations. *Science advances*, 3(4):e1602614, 2017.
- [16] Lu Lu, Pengzhan Jin, Guofei Pang, Zhongqiang Zhang, and George Em Karniadakis. Learning nonlinear operators via deeponet based on the universal approximation theorem of operators. *Nature machine intelligence*, 3(3):218–229, 2021.
- [17] Zongyi Li, Nikola Kovachki, Kamyar Azizzadenesheli, Burigede Liu, Kaushik Bhattacharya, Andrew Stuart, and Anima Anandkumar. Fourier neural operator for parametric partial differential equations. *arXiv preprint arXiv:2010.08895*, 2020.

[18] Kazuma Kobayashi, James Daniell, and Syed Bahauddin Alam. Improved generalization with deep neural operators for engineering systems: Path towards digital twin. *Engineering Applications of Artificial Intelligence*, 131:107844, 2024.

[19] Raisa Hossain, Farid Ahmed, Kazuma Kobayashi, Seid Koric, Diab Abueidda, and Syed Bahauddin Alam. Virtual sensing-enabled digital twin framework for real-time monitoring of nuclear systems leveraging deep neural operators. *npj Materials Degradation*, 9(1):21, 2025.

[20] Kazuma Kobayashi and Syed Bahauddin Alam. Deep neural operator-driven real-time inference to enable digital twin solutions for nuclear energy systems. *Scientific reports*, 14(1):2101, 2024.

[21] Waleed Diab and Mohammed Al-Kobaisi. Temporal neural operator for modeling time-dependent physical phenomena. *arXiv preprint arXiv:2504.20249*, 2025.

[22] Dibyajyoti Nayak and Somdatta Goswami. Ti-deeponet: Learnable time integration for stable long-term extrapolation. *arXiv preprint arXiv:2505.17341*, 2025.

[23] Johannes Brandstetter, Daniel Worrall, and Max Welling. Message passing neural pde solvers. *arXiv preprint arXiv:2202.03376*, 2022.

[24] Jayesh K Gupta and Johannes Brandstetter. Towards multi-spatiotemporal-scale generalized pde modeling. *arXiv preprint arXiv:2209.15616*, 2022.

[25] Phillip Lippe, Bas Veeling, Paris Perdikaris, Richard Turner, and Johannes Brandstetter. Pde-refiner: Achieving accurate long rollouts with neural pde solvers. *Advances in Neural Information Processing Systems*, 36:67398–67433, 2023.

[26] Franco Scarselli, Marco Gori, Ah Chung Tsoi, Markus Hagenbuchner, and Gabriele Monfardini. The graph neural network model. *IEEE transactions on neural networks*, 20(1):61–80, 2008.

[27] Junyan He, Shashank Kushwaha, Jaewan Park, Seid Koric, Diab Abueidda, and Iwona Jasiuk. Sequential deep operator networks (s-deeponet) for predicting full-field solutions under time-dependent loads. *Engineering Applications of Artificial Intelligence*, 127:107258, 2024.

[28] Ammar H Elsheikh, Swellam W Sharshir, Mohamed Abd Elaziz, Abd Elnaby Kabeel, Wang Guilan, and Zhang Haiou. Modeling of solar energy systems using artificial neural network: A comprehensive review. *Solar Energy*, 180:622–639, 2019.

[29] Mohammed Mudhsh, Emad MS El-Said, Ahmad O Aseeri, Rolla Almodfer, Mohamed Abd Elaziz, Samir M Elshamy, and Ammar H Elsheikh. Modelling of thermo-hydraulic behavior of a helical heat exchanger using machine learning model and fire hawk optimizer. *Case Studies in Thermal Engineering*, 49:103294, 2023.

[30] Emad Ghandourah, YS Prasanna, Ammar H Elsheikh, Essam B Moustafa, Manabu Fujii, and Sandip S Deshmukh. Performance prediction of aluminum and polycarbonate solar stills with air cavity using an optimized neural network model by golden jackal optimizer. *Case Studies in Thermal Engineering*, 47:103055, 2023.

[31] Ammar H Elsheikh, Emad MS El-Said, Mohamed Abd Elaziz, Manabu Fujii, and Hamed R El-Tahan. Water distillation tower: Experimental investigation, economic assessment, and performance prediction using optimized machine-learning model. *Journal of Cleaner Production*, 388:135896, 2023.

[32] Gokul Chandrasekaran, Neelam Sanjeev Kumar, Gowrishankar V, Neeraj Priyadarshi, and Baseem Khan. Iot enabled smart solar water heater system using real time thingspeak iot platform. *IET Renewable Power Generation*, 19(1):e12760, 2025.

[33] Kazuma Kobayashi, Samrendra Roy, Seid Koric, Diab Abueidda, and Syed Bahauddin Alam. From proxies to fields: Spatiotemporal reconstruction of global radiation from sparse sensor sequences. *arXiv preprint arXiv:2506.12045*, 2025.

[34] H Mavromichalaki, Athanasios Papaioannou, Christina Plainaki, C Sarlanis, G Souvatzoglou, M Gerontidou, M Papailiou, E Eroshenko, A Belov, V Yanke, et al. Applications and usage of the real-time neutron monitor database. *Advances in Space Research*, 47(12):2210–2222, 2011.

[35] NMDB Database. Nmdb: The neutron monitor database. Real-Time Database for high-resolution Neutron Monitor measurements. Accessed: 2024-12-03.

[36] Yosuke Iwamoto, Shintaro Hashimoto, Tatsuhiko Sato, Norihiro Matsuda, Satoshi Kunieda, Yurdunaz Çelik, Naoya Furutachi, and Koji Niita. Benchmark study of particle and heavy-ion transport code system using shielding integral benchmark archive and database for accelerator-shielding experiments. *Journal of Nuclear Science and Technology*, 59(5):665–675, 2022.

[37] Tatsuhiko Sato. Analytical model for estimating terrestrial cosmic ray fluxes nearly anytime and anywhere in the world: Extension of parma/expacs. *Plos one*, 10(12):e0144679, 2015.

- [38] Tatsuhiko Sato. Analytical model for estimating the zenith angle dependence of terrestrial cosmic ray fluxes. *PLoS one*, 11(8):e0160390, 2016.
- [39] Japan Atomic Energy Agency. EXPACS: EXcel-based program for calculating atmospheric cosmic-ray spectrum. <http://phits.jaea.go.jp/expacs/>. Accessed: November 4, 2024.
- [40] Tianping Chen and Hong Chen. Universal approximation to nonlinear operators by neural networks with arbitrary activation functions and its application to dynamical systems. *IEEE transactions on neural networks*, 6(4):911–917, 1995.
- [41] Sepp Hochreiter and Jürgen Schmidhuber. Long short-term memory. *Neural computation*, 9(8):1735–1780, 1997.
- [42] Junyoung Chung, Caglar Gulcehre, KyungHyun Cho, and Yoshua Bengio. Empirical evaluation of gated recurrent neural networks on sequence modeling. *arXiv preprint arXiv:1412.3555*, 2014.
- [43] Ashish Vaswani, Noam Shazeer, Niki Parmar, Jakob Uszkoreit, Llion Jones, Aidan N Gomez, Łukasz Kaiser, and Illia Polosukhin. Attention is all you need. *Advances in neural information processing systems*, 30, 2017.
- [44] Kurt Hornik, Maxwell Stinchcombe, and Halbert White. Multilayer feedforward networks are universal approximators. *Neural networks*, 2(5):359–366, 1989.